The thermodynamic stability of the Cassie–Baxter regime determined by the geometric parameters of hierarchical superhydrophobic surfaces

K. Maghsoudi, G. Momen, R. Jafari*

Department of Applied Sciences, University of Quebec in Chicoutimi (UQAC)

555, boul. de l'Université, Chicoutimi, Québec, G7H 2B1, Canada

** E-mail: Khosrow.maghsoudi1@uqac.ca*

Abstract

Understanding the geometric parameters of hierarchical superhydrophobic surfaces and their impact on the thermodynamic stability of the Cassie-Baxter regime are invaluable for surface wettability–related applications. Herein, we fabricated hierarchical micro-microstructured silicone rubber surfaces having superhydrophobic properties via an industrially applicable direct replication method. The mold inserts were fabricated using photochemical milling, laser ablation, and wet chemical etching to create different hierarchical levels. We calculated surface roughness ratios and equilibrium contact angles and considered the contribution of sub-microstructures in the wettability properties via physical and statistical analyses. Comparing the calculated theoretical wettability properties and experimental measurements revealed a good agreement among all samples because of the accurate predictions of the governing wetting regime. It was worthwhile insights into the design and fabrication of superhydrophobic structured surfaces. The presence of superimposed sub-microstructures produced desirable water-repellency properties because of the reduced solid–liquid contact area as low as 0.086. Given the primary importance of the Cassie–Wenzel wetting transition on the design and fabrication of superhydrophobic surfaces, we evaluated the thermodynamic persistence of the Cassie–Baxter regime by analyzing the energy barrier to be overcome by droplets with various volumes. Finally, we discuss the contribution of the dimensional parameters of microstructures on the stability of the Cassie–Baxter regime.

Keywords: Hierarchical structures, Superhydrophobicity, Geometric parameters, Contact angle, Wetting transition, Cassie–Wenzel transition

1. Introduction

The fabrication of superhydrophobic surfaces is of great importance to both academic and industrial fields. Superhydrophobic properties emerge by combining a low surface energy material and surface roughness. Such surfaces have demonstrated numerous potential uses, including, but not limited to, self-cleaning, anti-freezing and anti-icing, drag-reduction, and liquid transportation applications [1, 2]. Common techniques for creating superhydrophobic surfaces include chemical vapor deposition (CVD), layer-by-layer (LbL) deposition, sol-gel methods, electrochemical deposition, electrospinning and electro-spraying, and phase-separation techniques [3, 4]. However, templating or replication-based techniques have been the subject of many recent studies because of their utility in the mass production of superhydrophobic substrates [5-7]. The most common techniques include injection molding, compression molding, hot embossing or imprinting, and direct pouring. The essential factor in templating is the fabrication of a high-quality insert having the desired structures and its replication on a target substrate [5].

Many superhydrophobic materials produced by replication-based techniques possess an irregular or disordered surface roughness where the distribution of surface structures is random [8-10]. In such cases, the techniques to produce inserts are used to create irregular surface roughness on the insert surface. For example, wet chemical etching produces disordered surface roughness on metallic surfaces such as aluminum [11, 12], copper [13, 14], and steel [15, 16].

However, ordered surface structures provide myriad opportunities for studying the wettability properties via different phenomena. These studies are highly dependent on the roughness–property relationship, which includes the Cassie to Wenzel transition, water evaporation, droplet freezing, and dynamic droplet impacts. Ordered surface structures can be produced through replication-based techniques. Various techniques exist for fabricating metallic surfaces having desired well-defined surface structures; these include stamping, electrical discharge machining (EDM), electrochemical machining (ECM), micromechanical milling, laser ablation, and photochemical etching [17-19]. Laser ablation can be used either for creating disordered or ordered surface structures. The choice depends on the selected laser ablation processing parameters, including laser wavelength, laser pulse energy, pulse repetition rate, and, in particular, pulse duration [20, 21]. Ultrashort pulse duration is required to produce regular surface structures; however, this approach is considerably time-consuming and costly and, as such, is generally not applicable to industry.

Another technique for fabricating metal parts having well-defined surface structures is photochemical etching or photochemical machining (PCM) [22]. PCM combines photoresist imaging (photolithography) and wet chemical etching, which is widely used in industry [23]. This technique produces perforated metal components without burrs at low cost, at a relatively fast processing time, and with high precision [24]. PCM appears to be the most economical among the available techniques for producing stainless-steel perforated sheets [25]. These factors make PCM a good candidate for producing surface structures on metallic sheets as precise inserts to fabricate microstructured superhydrophobic surfaces.

Robust and durable non-wetting regimes, i.e., superhydrophobic surfaces with water-repelling properties, can be achieved through surfaces covered by hierarchical structures, including micro-nanostructures, micro-microstructures, micro-micro-nanostructures, and re-entrant morphologies [26-31]. Such surfaces can be produced by combining methods that produce various structures, including anodization, laser ablation, and micromachining [26, 28]. Zhou et al. [26] combined an etching method and anodization to replicate micro-nanostructures from an aluminum insert onto polycarbonate substrates. Noh et al. [20] created a multi-level hierarchy on a steel mold via laser ablation and fabricated a superhydrophobic PDMS through polymer casting. Huovinen et al. [29] fabricated micro-microstructured and micro-nanostructured aluminum molds by combining a microworking robot and anodization.

In addition to the challenges of fabricating such hierarchical structures on an insert surface, the proper filling of polymer materials into the hierarchical structures has been challenging [32-34]. For example, on dead-end inserts, not only is the fabrication of multi-level hierarchy a serious challenge because of the required expensive facilities [35], but polymer filling must also grapple with fast cooling and undesired shrinkage [34]. Hierarchical structures possess a higher surface-to-volume ratio leading to faster cooling of the molten polymer. Moreover, the sub-microstructures create larger capillary forces, making filling difficult.

Much research has focused on the effect of topographical parameters on the wetting behavior of superhydrophobic surfaces in relation to Cassie–Baxter and Wenzel wetting states [36-39]. However, few studies have considered hierarchical surface structures when calculating roughness. Huovinen et al. [29] fabricated a series of well-ordered hierarchical micro-microstructured surfaces and compared theoretical and experimental values of the wettability properties of the prepared surfaces. Grewal et al. [40] also produced micro-nanostructured hierarchical surfaces to study surface wetting performance, but the authors did not evaluate the effect of nanosized structures on the geometric dimensions. Hejazi et al. [41] believed that the wettability behavior of rough surfaces is much more complicated than to be predicted by Cassie–Baxter and Wenzel models only. They therefore developed a model to predict the wettability of hierarchical multi-scale surface structures. However, to our knowledge, no study has evaluated the wettability of micro-microstructured surfaces when combined with ordered and non-ordered structures.

On structured superhydrophobic surfaces, a water droplet is pinned on the top edge of the structures and, under pressure, bends toward the space between the structures. The intensity of the formed meniscus between the adjacent structures is critical in controlling the stability of the Cassie–Baxter wetting state [42]. The transition from a Cassie–Baxter to Wenzel state (a C–W transition) occurs by energetically overcoming this barrier. Various external stimuli can provoke this transition, including Laplace pressure, kinetic impact, thermal perturbation, and phase change [43]. These stimuli can be induced by various phenomena, such as a droplet impacting the surface, the evaporation of a static water droplet from the surface over time, vibration forces, acoustic waves, electric fields, and an increased water droplet volume (heavier droplet) [39, 44-47]. Several studies have focused on the effect of gravity on the transition behavior of various patterned surfaces [48, 49]. They highlighted the importance of the energy barrier, interfacial free energy, and the minimum required energy for the C–W transition.

From a Laplace Law point of view, relationships exist between droplet diameter and the pressure generated by its weight and the structured surface geometry. In other words, the transition from a Cassie–Baxter to a Wenzel wetting state is governed by the competition between the energy barrier and the external forces [50]. Hence, it is essential to understand and evaluate the thermodynamic stability of the produced structured superhydrophobic surfaces.

Here, we fabricate silicone rubber samples having hierarchically ordered surface structure morphology. The surface structures are fabricated via various inserts produced by multiple techniques. We aim to compare surface structures differing in terms of arrays and dimensions in regard to wettability characterization and superhydrophobicity. We use perforated sheets fabricated by photochemical milling and laser ablation to create micropillars as the first hierarchical level and wet chemically etched inserts for the second hierarchy level. Consequently, we achieve regular well-ordered structures having two hierarchical levels. The prepared surfaces' water contact angles (WCAs) are compared with predicted equilibrium contact angles, estimated according to thermodynamic analysis. We observe a consistency between the measured and calculated results. For the fabricated surfaces, we aim to determine the optimal design for achieving the highest WCA and the lowest contact angle hysteresis (CAH) values. We demonstrate how the various produced geometries differ in their behavior in regard to the pressure induced by water droplets of various volumes. Finally, we present and discuss the maximum pressures that each geometry can tolerate for various structural dimensions.

1.1. Wetting theories

On an ideal flat and chemically homogeneous solid surface, the equilibrium contact angle of a droplet is calculated using Young's equation [51]:

$$\cos\theta_Y = \frac{\gamma_{sv} - \gamma_{sl}}{\gamma_{lv}}, \qquad \textit{Eq. 1}$$

where γ is the interfacial energy per unit area of the corresponding solid, vapor, and liquid interfaces. Young's equation does not involve the surface roughness of solids. Therefore, the two wetting models of Wenzel and Cassie–Baxter are used to account for surface roughness for calculating surface contact angles. The suggested equation of Wenzel includes the surface roughness parameter for calculating the contact angle [52]:

$$r(\gamma_{sv} - \gamma_{sl}) = \gamma_{lv}\cos\theta_w, \qquad \textit{Eq. 2}$$

where r is the roughness parameter defined as the ratio of the actual wetted area to the projected wetted area and θ_w is Wenzel's contact angle. This equation can be modified as

$$\cos\theta_w = r\,\cos\theta\,. \qquad \textit{Eq. 3}$$

On a rough surface, r is always ≥ 1; hence, surface roughness intensifies surface hydrophilicity and hydrophobicity. The Wenzel model assumes a homogeneous wetting regime where the liquid thoroughly wets all the peaks and valleys of surface asperities. However, a composite wetting state is required to achieve superhydrophobicity. In the composite or heterogeneous wetting regime, air bubbles become trapped within the surface valleys; consequently, the water droplet cannot penetrate and remains atop the asperities. The result of this *fakir* state, in which the friction is reduced, is the droplet slipping easily along the surface [2]. In such case, the Cassie–Baxter model applies [53]:

$$\cos\theta_c = f_1\cos\theta_1 + f_2\cos\theta_2\,, \qquad \textit{Eq. 4}$$

where θ_c is Cassie–Baxter's contact angle and θ_i is the contact angle of phase i with a surface fraction of f_i. Given that $f_1 + f_2 = 1$ and the contact angle of a water droplet and air is 180°, i.e., cos 180° = −1, the modified Cassie–Baxter equation is [4]

$$\cos\theta_c = f_1 (\cos\theta_1 + 1) - 1 . \qquad \textit{Eq. 5}$$

More precisely, f_1 is defined as the proportion of the solid contact area with the liquid. It varies between 0, for no contact between the solid and liquid, and 1, where the Wenzel regime occurs (a full-contact state).

f and r are calculated according to the geometry of the surface structures (e.g., square, barrel-shaped, rectangular, or hexagonal) and the structure array (e.g., straight or staggered). For the geometries used in this paper, the f and r parameters are calculated using the following equations [5]:

$$r_{barrel-straight} = \frac{[(a+b)^2 + \pi a H]}{(a+b)^2}, \qquad \textit{Eq. 6}$$

$$f_{barrel-straight} = \frac{\pi a^2}{4(a+b)^2}, \qquad \textit{Eq. 7}$$

$$r_{barrel-staggered} = \frac{[\sqrt{3}(a+b)^2 + 2\pi a H]}{\sqrt{3}(a+b)^2}, \qquad \textit{Eq. 8}$$

$$f_{barrel-staggered} = \frac{\pi a^2}{2\sqrt{3}(a+b)^2}, \qquad \textit{Eq. 9}$$

$$r_{hexagonal-straight} = \frac{[(a+b)^2 + PH]}{(a+b)^2}, \qquad \textit{Eq. 10}$$

$$f_{hexagonal-straight} = \frac{3\sqrt{3}a^2}{8(a+b)^2}, \qquad \textit{Eq. 11}$$

where a, b, H, and P are the structure diameter, the distance between two adjacent structures, the structure height, and the circumference of a hexagon (Figure 1).

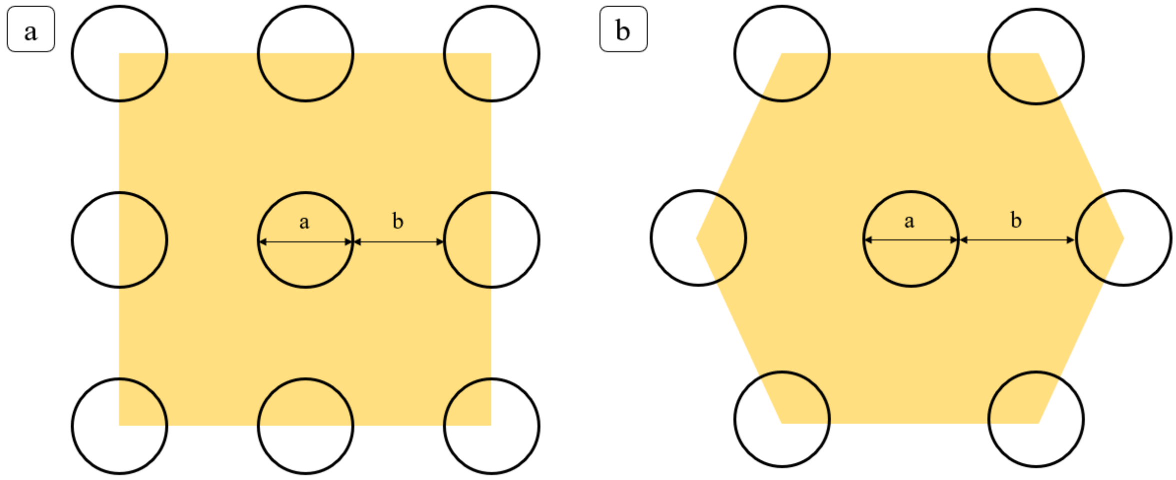

Figure 1. Schematic illustration of the two structural arrays and the associated dimensional parameters (a is the structure diameter and b is the distance between two adjacent structures)

Using these two surface roughness parameters, we can calculate the critical contact angle, which is derived from equalizing the Wenzel (*Eq. 3*) and Cassie–Baxter (*Eq. 5*) equations [5]:

$$\cos\theta_{crit} = \frac{f-1}{r-f}\,. \qquad Eq.\ 12$$

As θ_{crit} follows both regimes, when $\theta_Y < \theta_{crit}$, Wenzel and impregnated Cassie–Baxter states are more probable; otherwise, if $\theta_Y > \theta_{crit}$, then a stable Cassie–Baxter state is likelier. Therefore, θ_{crit} can be used to predict the behavior of a structured surface [29, 54].

2. Experimental procedure

2.1. Fabrication of mold inserts

The mold inserts were produced using various industrially applicable approaches. We fabricated the perforated stainless-steel (SS) inserts having microholes using either photochemical milling (M1 and M2 sheets) or laser ablation (M3 and M4 sheets). We controlled (with high precision) the dimensional parameters, including hole size, distance, and array. Moreover, the thickness of the used SS substrate defined the depth of the microholes.

In the photochemical milling of inserts, the hole taper or bevel was equally etched from both sides. This process leaves no burrs or rough edges, and the base metal remains consistent and unaltered. The holes were created with a size tolerance of ±15% of the material thickness. The laser ablation conditions were as follows: laser power of 100 W, laser pulse wavelength of 1064 nm, laser pulse duration of 100 µs, the laser fluence of 2.53 J/cm^2, the focused spot diameter of the laser beam was the same as the hole diameter, repetition rate of 1 Hz, with one pulse per hole.

We produced the inserts to create the second hierarchy of microstructures via the wet chemical etching method and used an aluminum alloy (A6061) with a chemical composition of Al 97.9 wt.%, Mg 1.0 wt.%, Si 0.60 wt.%, Cu 0.28 wt.%, and Cr 0.20 wt.%. The aluminum coupons were cleaned using acetone and distilled water for 20 min in an ultrasonic bath. After drying at 70 °C for 30 min, the coupons were immersed in an acid solution of 14.7 wt.% hydrochloric acid (HCl) for 2 h. The etched coupons were ultrasonically cleaned with distilled water for 40 min. Any residual acid and particles had to be fully removed from the prepared aluminum surfaces.

2.2. Fabrication of replicated structured surfaces

As schematically shown in Figure 2, we inserted the inserts into the mold to cast silicone rubber surfaces for the intended level of hierarchy. The single-level structures were only fabricated by inserting the perforated inserts (i.e., photochemically etched and laser-ablated stainless-steel sheets) into the mold cavity (a right rectangular prism cavity with dimensions of 25 × 25 × 6 mm). To create the second hierarchical level, we superimposed the wet chemically etched inserts onto the perforated inserts. Thus, the integrated mold inserts created dual-level hierarchical micro-microstructures.

We then carefully placed the mold inserts into the cavity to begin the compression molding. The machine consisted of two platens capable of applying up to ~200 kN pressing force. The temperature of each platen was digitally controllable, able to vary temperatures from ambient to 350 °C. Given our previous work on the optimization of processing parameters (i.e., molding pressure, mold temperature, and curing time) for the compression molding of silicone rubber [55], we selected these processing parameters: 20 MPa, 149 °C, and 4.7 min for the molding pressure, mold temperature, and curing time, respectively.

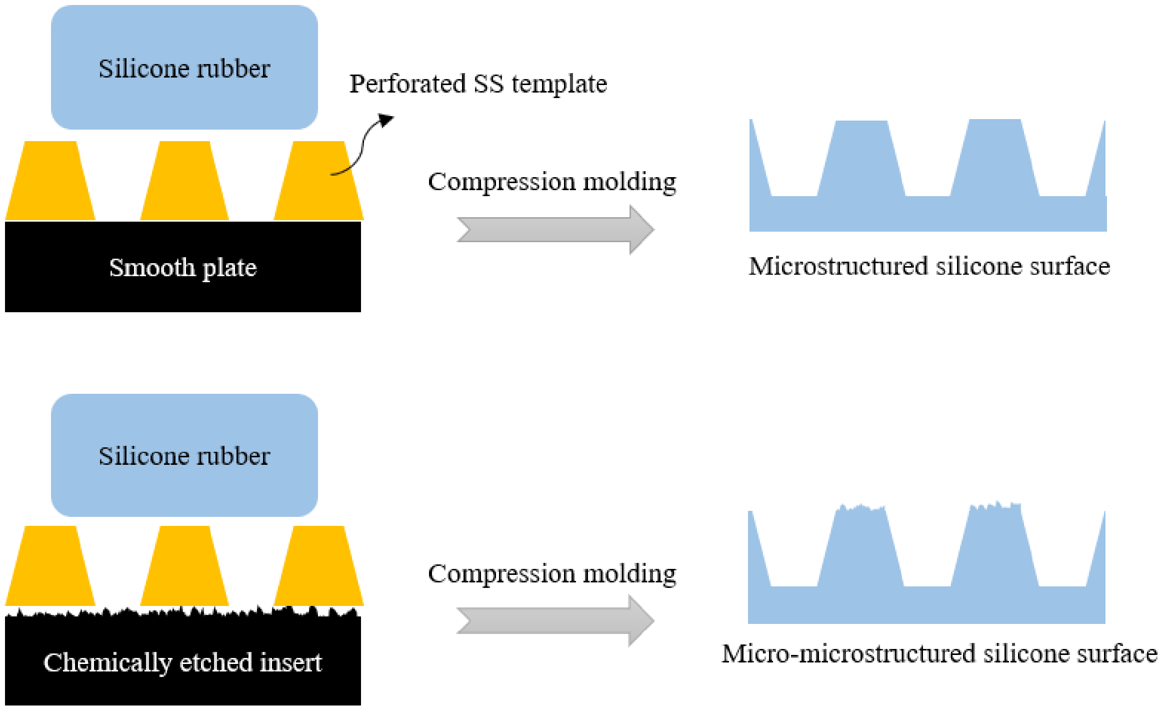

Figure 2. Schematic illustration of the two fabrication methods for preparing microstructured and micro-microstructured silicone surfaces using a compression molding system

2.3. Characterization of the replicated surfaces

Confocal laser scanning microscopy (CLSM; Profilm3D, Filmetrics, KLA Co., USA) and an optical microscope (Nikon, Eclipse, E600 POL) were used to measure the dimensions of the fabricated mold inserts and the replicated structures on the silicone rubber surfaces. The CLSM also evaluated the surface roughness parameters of the produced surfaces, including S_a (mean height), S_q (root mean square height), S_{sk} (skewness), and S_{ku} (kurtosis). the well-ordered surface structures were also observed using a scanning electron microscope (SEM) (JSM-6480 LV, JEOL Japan). SEM images were taken at a tilt angle of 35° to enhance the image quality. The WCA of the produced surfaces was measured using a Kruss™ DSA100 goniometer according to the sessile drop method at a fixed temperature of 24 ± 1.4 °C using a 4 μL deionized water droplet (with a surface tension of ~72.1 mN/m and a droplet diameter of 1.97 mm). The CAH equaled the difference between advancing and receding WCA when the water droplet was displaced over the surface using the needle tip. We repeated all measurements five times on each surface and report our results as the average and standard deviation. To evaluate the effect of hierarchical structures on the persistence of the Cassie–Baxter regime, we measured the WCA of the produced surfaces using 10 μL (diameter of 2.67 mm) and 20 μL (diameter of 3.37 mm) deionized water droplets. We previously showed in that all the fabricated surfaces have identical surface chemistry [8].

3. Results and discussion

3.1. Structured inserts

The dimensions of the produced inserts are shown in Table 1. To produce the first hierarchical level, we have four types of microholes that vary in dimensions and arrays, including straight cylindrical (M1), staggered conical (M2), straight conical (M3), and straight hexagonal (M4) perforations. We integrated the chemically etched inserts with the first two arrays to create dual-level hierarchical structures.

3.2. Geometric parameters of structured surfaces

Microholes of the perforated inserts were replicated as micropillars on the silicone rubber surface. Therefore, the straight cylindrical, staggered conical, straight conical, and straight hexagonal perforations produced corresponding frustum micropillars on the silicone rubber surfaces. The microbumps were created on top of the straight cylindrical and staggered conical micropillars by integrating the chemically etched inserts having micropits (denoted as MM structures).

The slight difference between the diameter and depth of the microholes and that of the replicated micropillars stems from the outward expansion produced by the release of internal stress when molding the silicone rubber [28]. M3 had the smallest hole diameter, so the high-viscosity silicone rubber material could not fill the microholes completely. Consequently, the height of the replicated micropillars was lower than microhole depth. In this case (M3), the replication fidelity was nonetheless acceptable and equal to ~95%.

Table 1. Dimensions of mold inserts and the associated replicated structured surfaces

	Dimensions of inserts (µm)				**Dimensions of replicated surfaces (µm)**			
	Microholes			Micropits	Micropillars			Microbumps
Type of structure*	Avg. depth	Avg. diameter	Avg. pitch	Avg. depth	Avg. height	Avg. diameter	Avg. pitch	Avg. height
M1	100	200	225	–	107 ± 2	204 ± 2	221 ± 1.5	–
MM1	100	200	225	10	108 ± 1.8	204 ± 2	221 ± 1.5	15.5 ± 0.5
M2	125	200–150	70–120	–	131.4 ± 1.3	208.7 ± 1.2 to 165.3 ± 2.3	117.6 ± 1.2 to 69.9 ± 2.6	–
MM2	125	200–150	70–120	12	132.6 ± 1.9	208.5 ± 1.1 to 172.8 ± 2.5	108.6 ± 1.7 to 67.6 ± 1.3	18.7 ± 3.3
M3	100	60–35	40–65	–	94.7 ± 1.2	64.3 ± 1.2 to 38.9 ± 0.5	62.1 ± 0.9 to 35.5 ± 0.6	–
M4	100	90–60	35–65	–	109.2 ± 0.9	93.4 ± 1.1 to 54.2 ± 3.8	71.3 ± 0.7 to 32.2 ± 0.9	–

* M1: straight cylindrical, M2: staggered conical, M3: straight conical, M4: straight hexagonal

3.3. Characterization of surface morphology

SEM images of the produced surfaces at various magnifications (Figure 3), along with the images of WCA and CAH (Figure 6), can help elucidate the relationship between the surface structures and wettability. A variable cross-sectional profile, i.e., diameter variation, was created across the material thickness in M1, i.e., wall of the holes, because of the photochemically etched holes. Therefore, re-entrant structures were fabricated after the demolding of the micropillars from the inserts. In theory, re-entrant structures cause relatively higher WCAs than those of micropillars having cylindrical structures (see the section on wetting theory). The positive effect of the re-entrant structures over the cylindrical structures has been discussed by researchers [10]. Toosi et al. [10] stated that the re-entrant structures ensure the entrapment of the required air pockets to achieve a stable Cassie–Baxter regime. This idea explains why M1 showed a stable Cassie–Baxter regime rather than the predicted regime, i.e., a Wenzel or impregnated Cassie–Baxter regime. Although we predicted a WCA of 147.0° for the M1 surface, we observed about 7° more than expected because of the re-entrant shape of the structures. To understand this difference between the theoretical and observed results, we can use sample M2 to illustrate. For M2, we observe a negligible difference between the theoretical and experimental WCA values (145.7° vs. 144.8°); the similarity of the results occurs because of the cylindrical shape of the microstructures.

The effect of hierarchical structures is evident particularly on CAH. The presence of micro- and sub-microstructures on top of the micropillars facilitated the dynamic motion of water droplets across surfaces having dual-level hierarchical structures. The WCAs of the single-level cylindrical micropillars (Figure 3a) and the dual-level hierarchical cylindrical micropillars (Figure 3b) differ by a small amount (154° and 158.6°, respectively). However, the CAHs differed markedly. Single-level micropillars produced a CAH of 20° ± 2°, indicating a non-water-repelling superhydrophobic behavior. A non-water-repelling superhydrophobic state occurs when the WCA of a surface is >150° and the CAH is >10°. This behavior is also known as the petal effect because of the superhydrophobicity yet high adhesive force of water droplets on the surfaces of red rose petals [57]. Consequently, the water droplet beads on the surface but cannot roll off. Dual-level micropillars, however, displayed a desirable water-repelling superhydrophobicity with a CAH of ~4°. This difference in behavior is attributed to the presence of micro- and sub-microstructures on the top of the micropillars; these structures reduce considerably the extent of the solid–liquid interface and produce minimal surface adhesion [58], thereby facilitating the dynamic motion of a water droplet that passes over the micropillars.

We observed similar results for the single-level and dual-level hierarchical conical micropillars (Figure 3c, d). The single-level conical micropillars produced a WCA and CAH of ~144.8° and ~28°, respectively, whereas the WCA and CAH of dual-level hierarchical micropillars were ~159.4° and ~3.5°, respectively. These observations vividly demonstrate the contribution of hierarchical micro-microstructures. Appropriate micro-microstructures can alter a design from being non-superhydrophobic to being a desirable superhydrophobic surface with marked water-repellency.

It is worth noting that compared to the single-level cylindrical micropillars (M1, with a WCA of ~154°), the single-level conical micropillars (M2) showed a considerably lower WCA (~144.8°). Although the diameters of the M2 pillar tops were less than those for M1 (165 µm vs. 204 µm), this lower WCA related mainly to the shorter pitch distance between the M2 micropillars (117.6 µm vs. 221 µm). Therefore, the solid–liquid area fraction (*f*) was considerably higher for the conical micropillars than for the cylindrical micropillars (0.310 vs. 0.181). These observations highlight the more significant influence of inter-structure distance than microstructure diameter. The inter-structure distance significantly affects the reducing solid–liquid contact area [59, 60].

We observed that single-level structures could produce a desirable water-repelling superhydrophobicity, although this occurrence is contingent on microstructure size. Microstructures having a diameter and pitch distance of <100 µm can produce a WCA >150° and a CAH <10° with only a single hierarchical level. Single-level conical micropillars (M3, Figure 3e) showed a higher WCA and lower CAH than the single-level hexagonal micropillars (M4, Figure 3f); we observed 167.0° and 5.2° for the WCA and CAH of M3 compared with 165.3° and 8.9°, respectively, for M4. This difference stems mainly from the smaller solid–liquid interface area on the conical structures having a smaller top diameter (~38.9 µm) than on the diagonal of hexagonal structures (~64.2 µm).

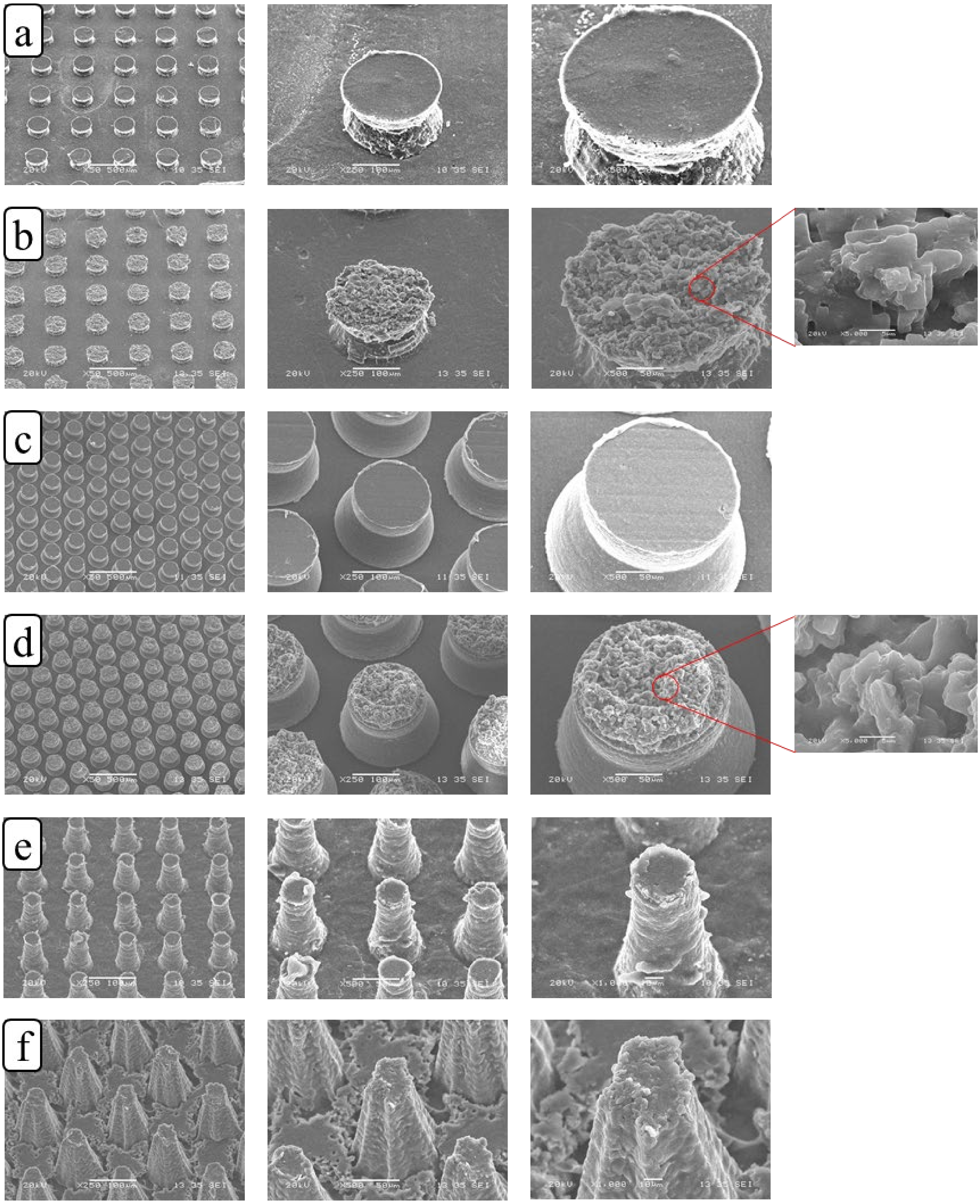

Figure 3. SEM images of samples (a) M1, (b) MM1, (c) M2, (d) MM2, (e) M3, and (f) M4 at various magnifications. The inset images present the surfaces at a higher magnification to highlight the hierarchical micro-microstructures on the corresponding surfaces

To further investigate the surface roughness of various structures, we used optical profilometry. Figure 4 displays the 2D and 3D surface profiles and 2D roughness values, including S_a (arithmetic mean height), S_q (root mean square height), S_{sk} (skewness), and S_{ku} (kurtosis). The sub-microstructures are clearly visible at the top of the MM1 and MM2 sample micropillars, whereas the pillar tops of samples M1 and M2 are almost smooth. The presence of the sub-microstructures evidently increased the height of the micropillars and surface roughness. We measured the roughness of a 100 × 100 µm area from a pillar top of the M1 and MM1 samples. The 2D root mean square (S_q) of the M1 pillar top was 0.69 µm, whereas that of the MM1 sample was 6.78 µm. When compared with the M1 and MM1 samples, we observed very similar roughness values for the M2 and MM2 pillar tops at 0.62 µm and 7.37 µm, respectively. This ~10× increase in the surface roughness of the pillar tops indicates why pillars superimposed with sub-microstructures offered better droplet roll-off properties.

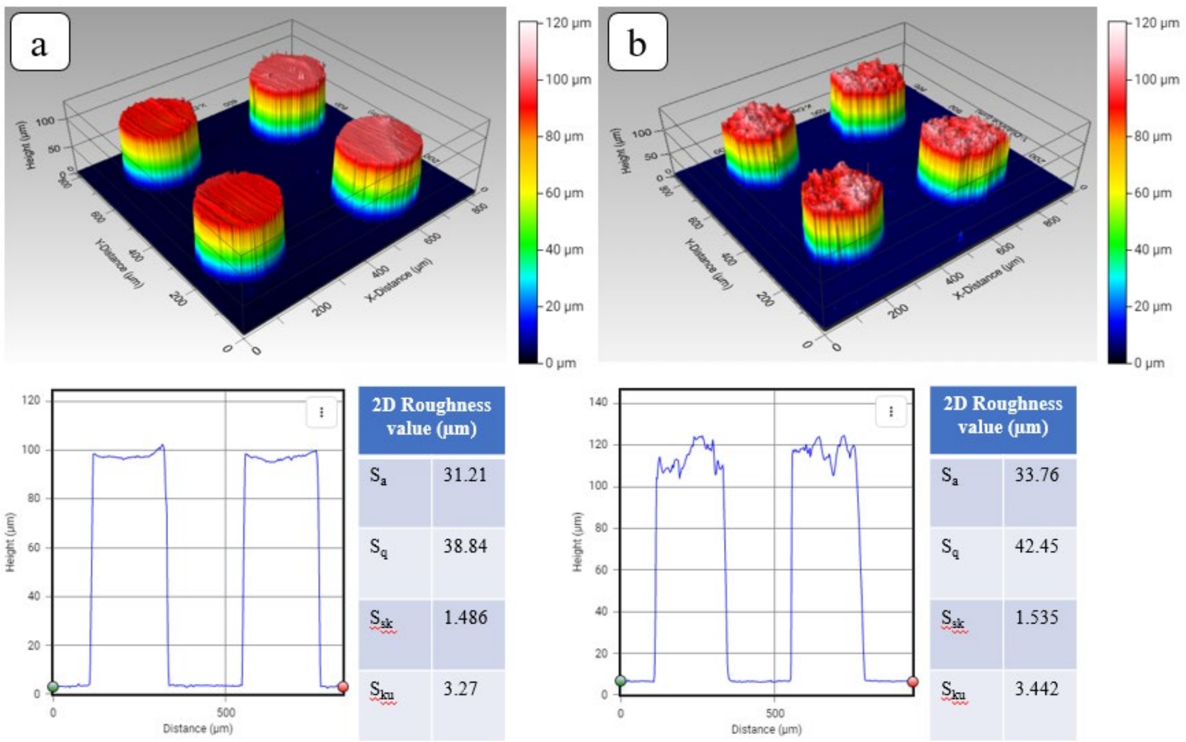

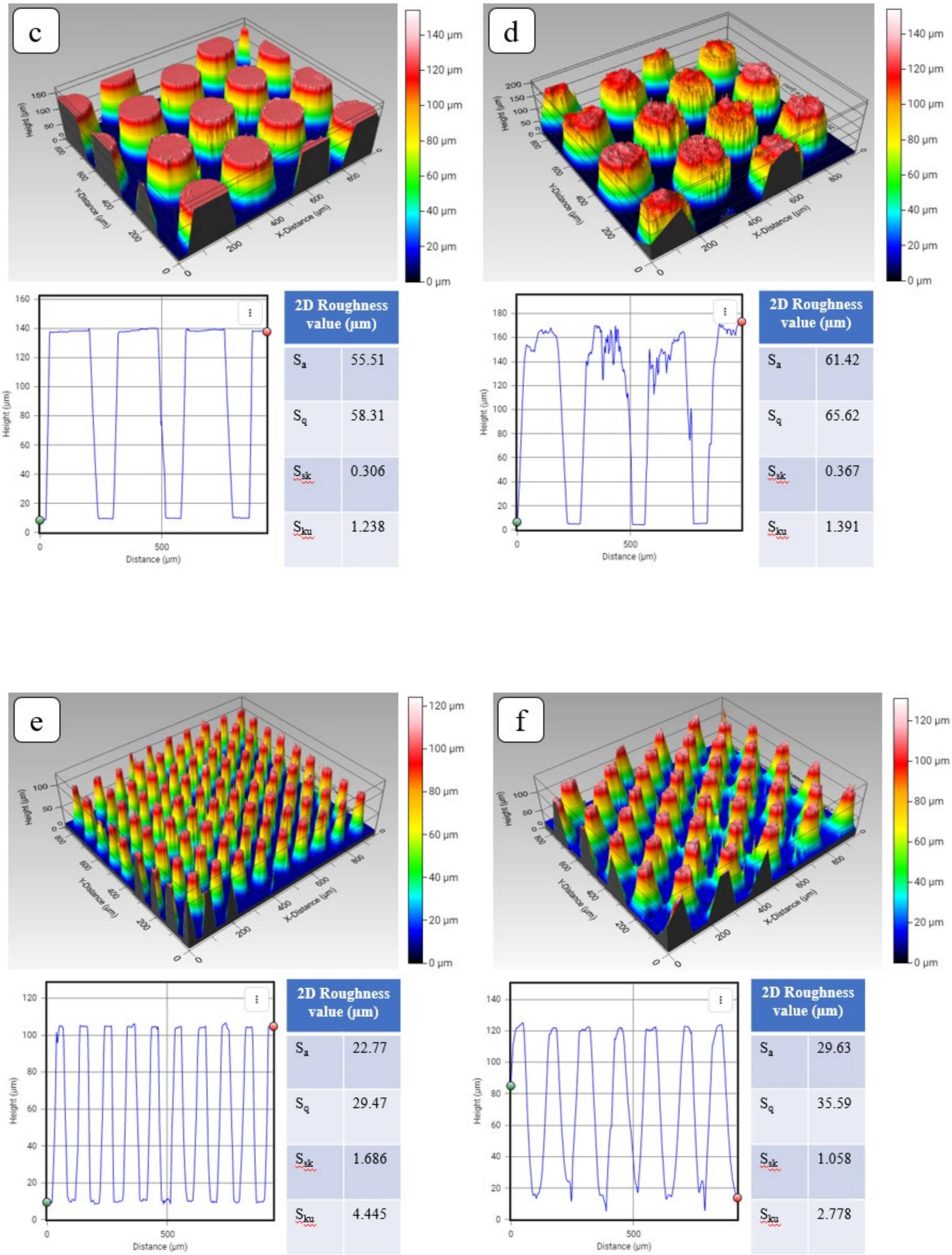

Figure 4. 3D and 2D profilometry images of (a) M1, (b) MM1, (c) M2, (d) MM2, (e) M3, and (f) M4 along with the 2D roughness values

3.4. Wetting properties

In many studies, structure shape is assumed to be the most common regular geometrical shape. For example, almost all geometries with a circular cross-section are assumed to be cylindrical or conical. In many cases, however, the produced geometrical shape is more complex than assumed. Thus, we calculated the roughness parameters of the produced structured surfaces according to their true geometrical shapes using the most precise equations. In equations 6–11, only the Wenzel parameter (*r*) changes for our structures; the equations of Cassie–Baxter parameter (*f*) remains unchanged (equations 7, 9, and 11). This occurs because the *f* parameter involves only the upper surface area and not the lateral surface area. To calculate Wenzel roughness parameters, we therefore used the following equations:

M1:

$$r_W = \frac{[(a+b)^2 + 2\pi(a+a\prime)\sqrt{(a-a\prime)^2+(\frac{H}{2})^2}\,]}{(a+b)^2}, \qquad \text{Eq. 13}$$

M2:

$$r_W = \frac{[\sqrt{3}(a+b)^2 + 2\pi\big(a+a'\big)\sqrt{(a-a')^2+H''^2} + 2\pi a H\prime]}{\sqrt{3}(a+b)^2}, \qquad \text{Eq. 14}$$

M3:

$$r_W = \frac{[(a+b)^2 + \pi(a+a\prime)\sqrt{(a-a\prime)^2+H^2}]}{(a+b)^2}, \qquad \text{Eq. 15}$$

M4:

$$r_W = \frac{[(a+b)^2 + (\frac{P_1+P_2}{2})\sqrt{(ap_2-ap_1)^2+H^2}]}{(a+b)^2}, \qquad \text{Eq. 16}$$

where *a*, *b*, *a'*, *H*, *H'*, *H''*, *P*, and *ap* are the smallest diameter pitch distance, largest diameter, total structure height, cylindrical section height, trapezoidal section height, hexagon circumference, and apothem of a hexagon (the distance from its center to the midpoint of one of its sides), respectively (Figure 5).

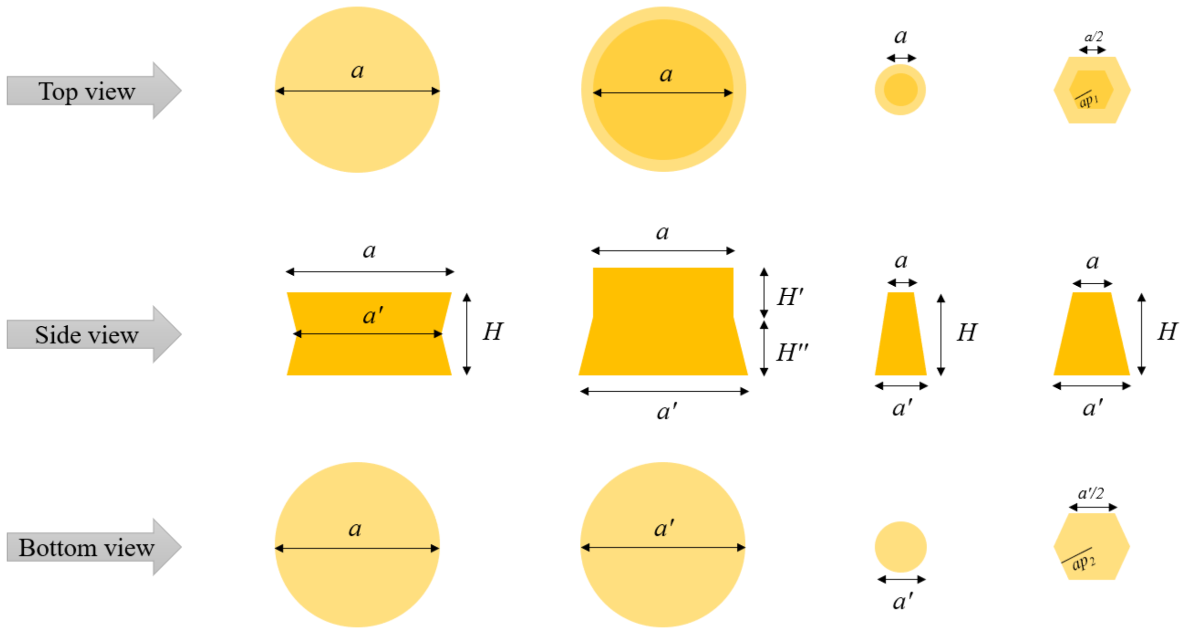

Figure 5. Schematic illustrations of the geometry and dimensions of the four fabricated microstructures; the ratios are the true dimensions.

Using the calculated roughness parameters (r_W and f), we determined each surface's critical contact angle (θ_{crit}). The expected wetting regime was determined according to the critical contact angle (note that $\theta_Y = 116.0°$ for silicone rubber). The theoretical WCA was then calculated for the corresponding predicted regime. The experimental WCA and CAH of the produced surfaces were also measured. Table 2 presents the theoretical and observational values of the wetting properties of the samples having various surface structure dimensions based on a true-shape assumption. Figure 6 displays the images of WCA and CAH for all surfaces.

Table 2. Roughness parameters and various contact angles of the produced surfaces based on true shape assumption

Sample	r_W	f	θ_{crit} (°)	Predicted regime	Theoretical WCA (°)	Experimental WCA (°)	CAH (°)
M1	1.91	0.181	118.2	Wenzel (Cassie)	147.0 (153.9)	154.0 ± 0.1	20 ± 2.3
MM1	–	0.086	–	–	162.1* / 161.4**	158.6 ± 0.3	4.1 ± 1.6
M2	2.86	0.310	105.7	Cassie–Baxter	145.7	144.8 ± 0.2	28 ± 2.6
MM2	–	0.109	–	–	160.0* / 159.5**	159.4 ± 0.3	3.5 ± 0.6
M3	4.42	0.117	102.8	Cassie–Baxter	159.2	167.0 ± 0.3	5.2 ± 1.3
M4	2.55	0.121	111.2	Cassie–Baxter	158.7	165.3 ± 0.2	8.9 ± 1.0

* Calculated based on physical analysis (Section 3.4.1)

** Calculated based on statistical analysis (Section 3.4.2)

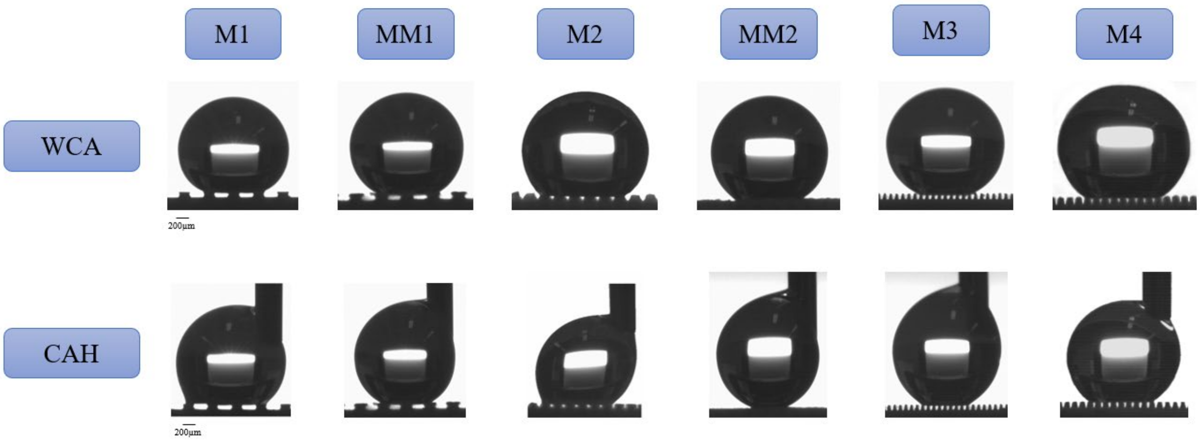

Figure 6. The WCA and CAH of the microstructured (M1, M2, M3, and M4) and micro-microstructured (MM1, MM2) surfaces

The theoretical and experimental results showed a good agreement among all samples because of the accurate predictions of the governing wetting regime. For all samples except M1, the governing regime was Cassie–Baxter. The theoretical WCA for M1 was 147.0° for a Wenzel or impregnated Cassie–Baxter state and 153.9° for a stable Cassie–Baxter state. The measured WCA for the M1 surface was 154.0°. Thus, the water droplet on M1 falls into an impregnated Cassie–Baxter regime and is not in a fully Wenzel state. This is also evident from the sample M1 image of its WCA (Figure 6).

We stated earlier that if $\theta_{crit} < \theta_Y$, the predicted wetting regime would be Cassie–Baxter. It can be mathematically concluded that the greater the difference between θ_{crit} and θ_Y, the more stable the Cassie–Baxter regime. Sample M3, having the lowest θ_{crit}, produced the highest WCA and lowest CAH without hierarchical structures.

The hierarchical dual-level structures affected the non-wetting properties of the surfaces having single-level structures. When we compare samples M1 and MM1, we note that the hierarchical structures considerably decreased the CAH from 20° (a non-water-repellent state) to 4.1° (a desirable water-repellent state). Samples M2 and MM2 demonstrated the same behavior. The microbumps on the micropillar tops not only produced a WCA >150° but also produced a CAH as low as 3.5°. Pinning effects increase hysteresis. Given that the geometrical parameters of the pairs of M1 - MM1 and M2 - MM2 are identical, the high CAHs of samples M1 and M2 are attributed to the extensive solid–liquid contact line atop the pillars. Therefore, the superimposed sub-microstructures markedly reduced the solid–liquid contact line and decreased the CAH remarkably.

More importantly, we observed that an appropriate set of single-level structures could produce the desired superhydrophobic behavior with water-repellent properties. Samples M3 and M4 both produced a WCA >160° and CAH <10°. As mentioned above, M3 demonstrated the best superhydrophobicity. These favorable non-wetting properties (ultra-high WCA and ultra-low CAH) relate to the very limited solid–liquid contact area. The *f* value of 0.117 represents this limited contact area. Therefore, only 11.7% of the surface area was in contact with the water droplet, and 88.3% was in contact with air.

The presence of dual-level hierarchical structures dramatically reduced the extent of the solid–liquid interface, which directly affects drag reduction during droplet motion over the structures. Consequently, the surfaces with hierarchical structures (MM1 and MM2) produced an extremely low CAH, with even lower values than those for M3 and M4. Therefore, instead of controlling/reducing micropillar dimensions, which can be associated with challenges in processing and elevated fabrication costs, micropillars can be superimposed with hierarchical structures to enhance superhydrophobic properties of surfaces.

We calculated the theoretical WCA for a wide range of structural dimensions using the derived equations of *r* and *f* for each surface geometry (Figure 7). For each surface geometry, we assumed 10 micropillar top diameters of 10 μm to 100 μm. Then, we considered various pitch-to-diameter ratios (b/a) from 0.5 to 3 at 0.1 intervals. All other dimensional parameters were held constant, e.g., structure height, or were altered proportionally by diameter. This approach provided a rational and comprehensive design of the fabrication procedure to achieve superhydrophobic structured surfaces.

Depending on whether the prediction was based on Wenzel or Cassie–Baxter states, we obtained two theoretical WCAs for each case. We selected the WCA in regard to the θ_{crit}, i.e., as long as $\theta_{crit} < \theta_Y$, the WCA calculated from Cassie–Baxter equation was valid. Otherwise, when, i.e., $\theta_{crit} > \theta_Y$, we selected the WCA calculated for the Wenzel equation. Therefore, in many cases, we observed a maximum value for the achievable WCA associated with a particular b/a; this ratio can therefore be considered a key element in the design of superhydrophobic surfaces. In Figure 7a, for instance, the maximum WCA (156.4°) was obtained for b/a = 1.3 and a microstructure diameter of 100 μm. As the diameter decreased, the transition from Cassie–Baxter to Wenzel occurred at a higher WCA, continuing until the 30 μm pillar diameter. For the 20 μm and 10 μm pillar diameters (overlapping curves), even at the highest b/a (= 3), we observed no decrease in WCA. Comparing the transition WCAs provides insight into the wettability behavior of the different geometries. Whereas the transition from a Cassie–Baxter to Wenzel state (maximum WCA on each curve) started at a b/a of 1.3 for the M1 geometry, the transition occurred at a b/a of 1.7, 1.8, and 1.0 for the M2, M3, and M4 geometries, respectively. Therefore, the M3 geometry was the best in terms of the persistence of the Cassie–Baxter regime.

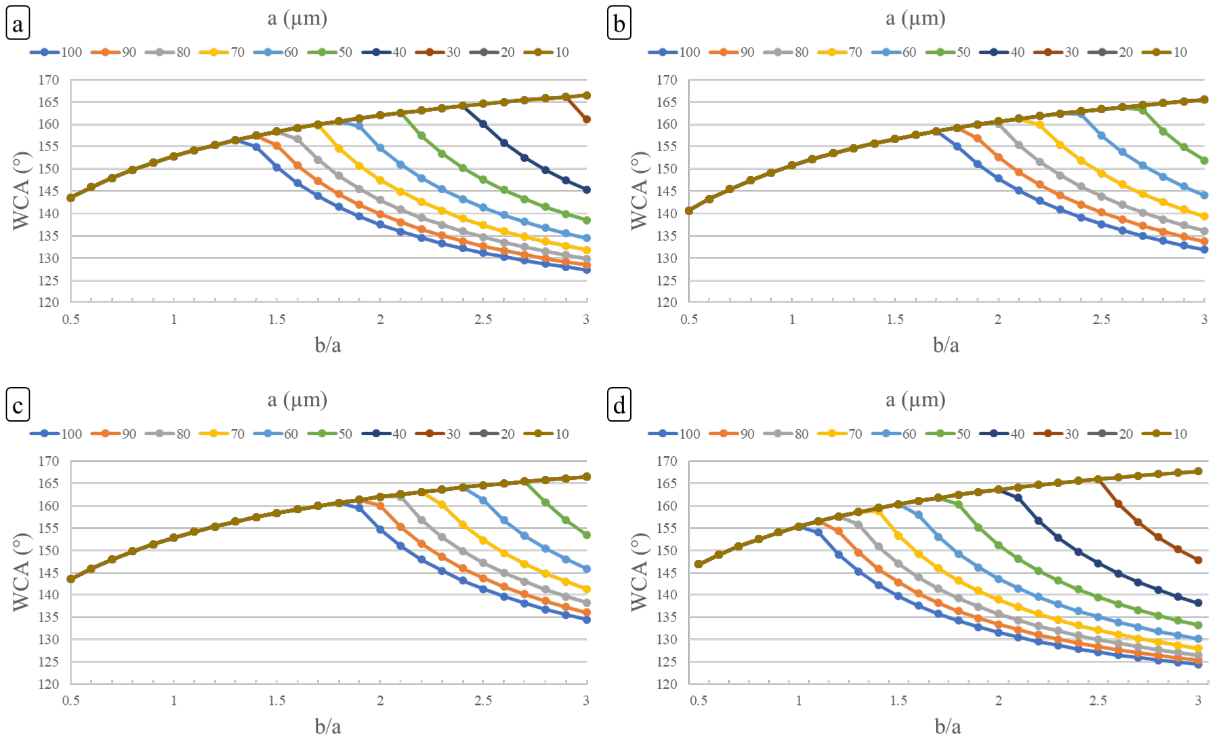

Figure 7. Theoretical WCA as a function of the pitch-to-diameter ratio (b/a) for various (a), (b), (c) micropillar top diameteres of M1, M2, M3, respectively, and (d) long diagonal of hexagonal of M4 geometries

3.5. Influence of hierarchical micro-microstructures on wettability properties

3.5.1. Physical analysis

To predict the theoretical WCA of the hierarchical micro-microstructured surfaces (MM1 and MM2), we must calculate the solid–liquid contact area, i.e., the f parameter in the Cassie–Baxter equation, for those structures. Therefore, f for the second-level hierarchy of microstructures must be calculated. The calculation of total f for the surface involves multiplying f_M and f_{MM}, where indexes 1 and 2 represent micropillars and disordered superimposed microstructures, respectively. However, calculating such a value for the second-level hierarchy of microstructures—being randomly textured—is not as straightforward as that for ordered microstructures. Here, we propose a state-of-the-art calculation based on the trapped air volume between the microstructures. We obtain the air volume from the profilometry analysis of a 130

× 130 µm area atop the MM1 micropillars and an 85 × 85 µm area on top of the MM2 micropillars. Therefore, assuming the air pockets have a pyramidal shape and using the root mean square (S_q) as pyramid height, we can calculate the surface area of the trapped air in contact with the liquid. Given that on a surface $f_1 + f_2 = 1$, we can obtain the solid contact area with liquid. Consequently, we calculated each hierarchical micro-microstructure's total f (f_{total}) by multiplying f for each hierarchical level. Table 3 presents the results for MM1 and MM2.

Table 3. The values for the calculation of the proportion of solid–liquid contact area for the hierarchical micro-microstructured surfaces.

Sample	Trapped air volume (µm³)	Root mean square (S_q) (µm)	Surface area of the trapped air (µm²)*	Ratio of air-liquid contact area (f_1)	Ratio of solid–liquid contact area ($f_2 = f_{MM}$)	$f_{total} = (f_M \times f_{MM})$**	Theoretical WCA (°)
MM1	16,772	5.693	8,838.2	0.523	0.477	0.086	162.1
MM2	6,453	4.135	4,681.7	0.648	0.352	0.109	160.0

* The volume of a pyramid with a base surface area of A and height of h equals to $V = \frac{Ah}{3}$

** f_M is given in Table 2

3.5.2. Statistical analysis

Our second method for predicting the WCA of the hierarchical micro-microstructured surfaces (MM1 and MM2) relied on a statistical approach. Khandoker et al. [56] demonstrated that this approach could predict the WCA for surfaces in a Cassie–Baxter state. We can rewrite the Cassie equation, i.e., the statistical Cassie contact angle, as

$$\cos\theta^*_{C,stat} = \frac{1}{D^*_{stat}}\left[\left(1 + \frac{S_{dr}}{100}\right)\cos\theta - D^*_{stat} + 1\right]. \qquad \textit{Eq. 17}$$

S_{dr} is defined as the developed interfacial area ratio and is obtained from profilometry. However, the relationship between S_{dr} and r_W can be expressed as

$$r_W \approx 1 + 0.01 S_{dr}\ . \qquad \textit{Eq. 18}$$

D^*_{stat}, known as the statistical porosity parameter, is defined especially for disordered surface structures and is calculated as

$$D^*_{stat} = \left(\frac{RS_m}{S_{al}}\right)^2, \qquad \textit{Eq. 19}$$

where RS_m characterizes the average spacing between successive peaks in a random height profile [56]. To calculate RS_m, if the structure height is >10% of R_t (maximum peak-to-valley height) and its width is >1% of the total scanned length, the structure is considered a peak. Thus, RS_m can be considered as a statistical center-to-center distance. S_{al} is the autocorrelation function and can be considered as the statistical average structure size. Table 4 presents the statistical parameters and calculated WCA for the hierarchical micro-microstructures.

Table 4. Statistical parameters for calculating the WCA of the hierarchical micro-microstructured surfaces

Sample	RS_m	S_{al}	D^*_{stat}	S_{dr}	$\cos\theta^*_{C,stat}$	$\theta^*_{C,stat}$
MM1	3.8	3.33	1.30	113%	−0.948	161.4
MM2	6.1	3.44	3.14	83%	−0.937	159.5

3.6. Thermodynamic stability of the Cassie–Baxter state and its breakdown conditions

Wetting transition is a key element in the design and fabrication of superhydrophobic surfaces. Although the abovementioned thermodynamic equations show the requirements for fabricating superhydrophobic surfaces, they do not elucidate the stability of the wetting states. An energy barrier separates the Cassie–Baxter state from the Wenzel state [39]. Therefore, this energy barrier can prevent this transition depending on the geometry parameters of a given structured superhydrophobic surface. The relationship between the volume of a settling droplet on a superhydrophobic surface and the WCA of the surface can be expressed as [39]

$$\frac{G_c}{\sqrt[3]{9\pi}V^{2/3}\gamma_{lv}} = (1-\cos\theta_c)^{2/3}(2+\cos\theta_c)^{1/3}\,, \qquad \textit{Eq. 20}$$

where V is the droplet volume, γ_{lv} is the liquid surface tension, θ_c is the Cassie–Baxter WCA, and G_c is the energy of the droplet in the Cassie–Baxter state, which is defined as

$$G_c = S_c\gamma_{lv} - \cos\theta_c A_c\,, \qquad \textit{Eq. 21}$$

where S_c is the surface area of liquid–air contact and A_c is the projected solid–liquid contact area. It is assumed that gravity is negligible; thus, the droplet shape is spherical. From *Eq. 20*, increasing the droplet volume reduces the WCA, thereby favoring the transition from a Cassie–Baxter state to a Wenzel state at a lower energy level.

The WCAs of the larger droplets with the ordered, structured surfaces are presented in Figure 8. We used 10 and 20 µL droplets having diameters of 2.67 and 3.36 mm, respectively. The WCA decreased with increasing droplet size. Therefore, M1 and M2 samples showed lower WCAs for droplets larger than 4 µL. The hierarchically micro-microstructured surfaces, however, retained their superhydrophobicity against the larger droplets. MM1 preserved the Cassie–Baxter state with the 10 µL droplet, whereas the transition to the Wenzel regime occurred when the 20 µL droplet was used. Comparing the results for M2 and MM2, we observe that the micropillars covered by the hierarchical microstructures prevented considerably the water droplet from intruding into the structures. Therefore, the liquid–air interface does not go further down into the cavities between the structures. The air cavities were evident on the MM2 surface when a 10 μL droplet was placed on the surface, whereas the air cavities were almost completely filled with water when a 10 μL droplet was placed on the M2 surface. Although the 20 μL droplet intruded partially into the MM2 surface structures at the center, it did not completely spread over the surface and maintained its spherical shape. In contrast, the 20 μL droplet collapsed and produced a WCA of ~130.4° on the M2 surface. Samples M3 and M4 showed an excellent persistence of the Cassie–Baxter state. Regardless of droplet volume, the water droplets did not penetrate the surface structures, and the air pockets were clearly evident.

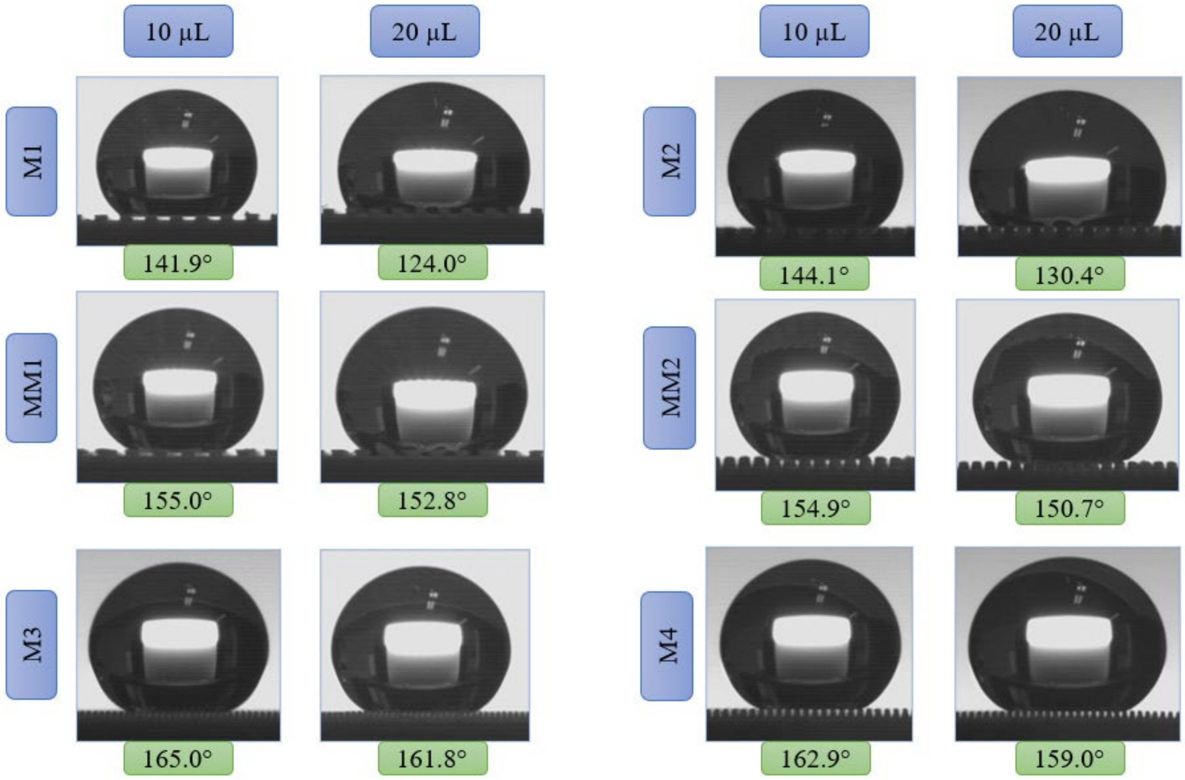

Figure 8. Images of water droplets on various surface structure with a volume of 10 μL and 20 μL

For a Cassie–Baxter state to be stable, the surface tension must prevent a water droplet from penetrating the air cavity. The water droplet applies a pressure of P generated by its weight, and the surface tension force (F_s) applied to the interface triple line opposes the water droplet weight. P is calculated as [42]

$$P = \frac{W}{S_{air}} = \frac{\rho g h S_{air}}{S_{air}} = \rho g h \,, \qquad \textit{Eq. 22}$$

where ρ is the density of water, g is the gravitational acceleration, h is the height of the water droplet, and S_{air} is the surface of the liquid–air interface. However, F_s can be calculated using [42]

$$F_s = \gamma l \cos(\theta_Y - \psi + 90°) \,, \qquad \textit{Eq. 23}$$

where γ is the surface tension of water, l is the length of the triple line, θ_Y is the Young contact angle, and ψ is the angle between the structure's bottom and wall (as shown in Figure 9).

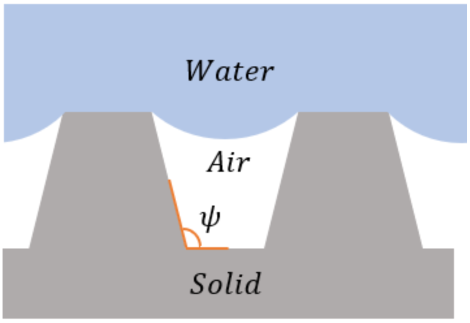

Figure 9. The solid–liquid–air composite on a structured surface with ψ as the angle between the structure's bottom and wall

Given an equilibrium between W and F_s, the maximum droplet pressure able to be countered by surface tension is

$$P_{max} = \frac{-\gamma l \cos(\theta_Y - \psi + 90°)}{S_{air}} \,. \qquad \textit{Eq. 24}$$

We calculated P_{max} for different single-level structure geometries and compared them with the applied pressure—the pressure related to the weight of the water droplet (4, 10, or 20 µL) (Table 5). We selected these three volumes in relation to the capillary length of a water droplet, calculated as $l = \sqrt{\frac{\gamma}{\rho g}}$. Thus, the capillary length for a water droplet having a surface tension of γ = 72.8 mN/m and a density of ρ = 997 kg/m^3 is 2.73 mm, which corresponds to a 10 µL water droplet.

Table 5. The calculated P_{max} for various single-level structure geometries

Sample	ψ (°)	$\cos(\theta_Y - \psi + 90°)$	l (m) × 10^6	S_{air} (m^2) × 10^6	P_{max} (Pa)
M1	123 (57)	0.12 (−0.86)	πa = 640.88	$(a + b)^2 - \pi(a/2)^2$ = 0.147940	−38.4 (270.3)
M2	114	−0.035	πa = 519.31	$(a + b)^2 - \pi a^2/2\sqrt{3}$= 0.051418	25.7
M3	102	−0.24	πa = 122.21	$(a + b)^2 - \pi(a/2)^2$ = 0.009013	288.6
M4	108	−0.14	3a = 162.6	$(a + b)^2 - 3\sqrt{3}a^2/8$= 0.014097	116.9

The first conclusion drawn from the results is the negative amount of pressure for M1 sample, which stems from $\psi > \theta_Y$. In such a condition, the droplet penetrates the structures, and a fully

Wenzel state is dominant. If ψ is considered as the re-entrant angle for micropillars on M1, i.e., 57°, P_{max} is 270.3 Pa. For M1, neither assumption is apparently valid. In the first scenario, i.e., the fully Wenzel state, we observed that M1 is in a Cassie–Baxter or impregnated Cassie–Baxter state for the 4 µL and 10 µL droplets. On the other hand, i.e., assuming the re-entrant angle for ψ and the pressure of droplets of various volumes (Table 6), even the largest droplet has a much smaller pressure than P_{max}, meaning that no penetration may occur. However, we did not observe this predicted state. Rather, the 20 µL droplet was thoroughly in a Wenzel state. This contradiction can only be interpreted by the exceptional geometry of the M1 micropillars, a combination of ordinary conical and re-entrant frustums. The results for M2, however, perfectly match our observations. We calculated a maximum pressure of 25.7 Pa for overcoming the M2 geometry. Whereas the 4 µL droplet was in an impregnated Cassie–Baxter regime, the 10 and 20 µL droplets sagged between the surface structures, as the pressures generated by their weights were greater than P_{max}.

Table 6. The pressure generated by various droplet volumes because of their weights

Droplet volume (µL)	**Droplet diameter (mm)**	**Pressure (Pa)**
4	1.97	19.2
10	2.67	26.1
20	3.37	32.9

We observed quite interesting results for the M3 and M4 samples. The P_{max} for both surfaces was much greater than the pressure generated by the droplets, i.e., 288.6 and 116.9 Pa, respectively. Therefore, no droplet penetrated the asperities of the M3 and M4 samples. M3 and M4 samples could withstand the pressure generated by 24 mm and 12 mm water columns, respectively. If we assume that such large volumes of water can still shape a droplet, the corresponding water droplet volumes having these heights, i.e., diameter, are 7.2 and 0.9 mL, respectively.

To demonstrate the persistence of the Cassie–Baxter state for the M2, M3, M4 geometries, we can plot the maximum required pressure for a water droplet to intrude the structures as a function of the surface's structural dimensions (Figure 10). We selected diameters of 10 to 100 µm at 10 µm steps for micropillar geometries and selected the same values for the long diagonal for the hexagonal geometries. For each a value, pitch distance (b) was $a/2$ to $3a$ to include a reasonable range of structures.

Two key observations are observed in Figure 10. First, the maximum P_{max} is observed for the M3 geometry (Figure 10b), which occurs as this surface has the lowest length of triple line and lowest ψ. These values reflect the minimal available air surface for the water droplet to apply its weight force; therefore, the required intrusion pressure is maximized. It is worth noting that whereas M3 shows a P_{max} of almost 4500 Pa for a = 10 µm and b = 5 µm, the M2 geometry attains only 1000 Pa, even at the smallest a and b values. Moreover, M4 has only a P_{max} >1000 Pa for four designs having a = 10 µm.

Another key observation relates to minimum P_{max} values. M3 demonstrates the best performance, having the lowest P_{max} of ~44 Pa for a = 100 µm and b = 300 µm. This pressure is theoretically greater than the pressure generated by a 20 µL droplet. P_{max} did not drop below 100 Pa for a values of 10, 20, 30, and 40 µm. M2, on the other hand, shows a P_{max} <100 Pa after a specific value of b at each a. At a >60 µm, regardless of the b value, P_{max} is <100 Pa for M2. Given that the pressure generated by a 4 µL droplet is 19.2 Pa, P_{max} for the M2 geometry falls below this value at a = 30 µm and b = 86 µm. M4 geometry maintains a P_{max} of 100 Pa for almost all designs with a = 10 and 20 µm. The lowest P_{max} for the M4 geometry is 19.6 Pa, which is very close to the pressure generated by a 4 µL droplet. The energy barrier for the Cassie–Baxter to Wenzel wetting transition is inversely proportional to pitch distance ($\Delta E \propto \frac{1}{b}$) [50]. This energy barrier, which is directly proportional to P_{max}, prevents the water droplet from penetrating the structures by acting in an upward direction. Therefore, increasing the pitch distance lowers significantly the energy required for the Cassie–Baxter to Wenzel wetting transition.

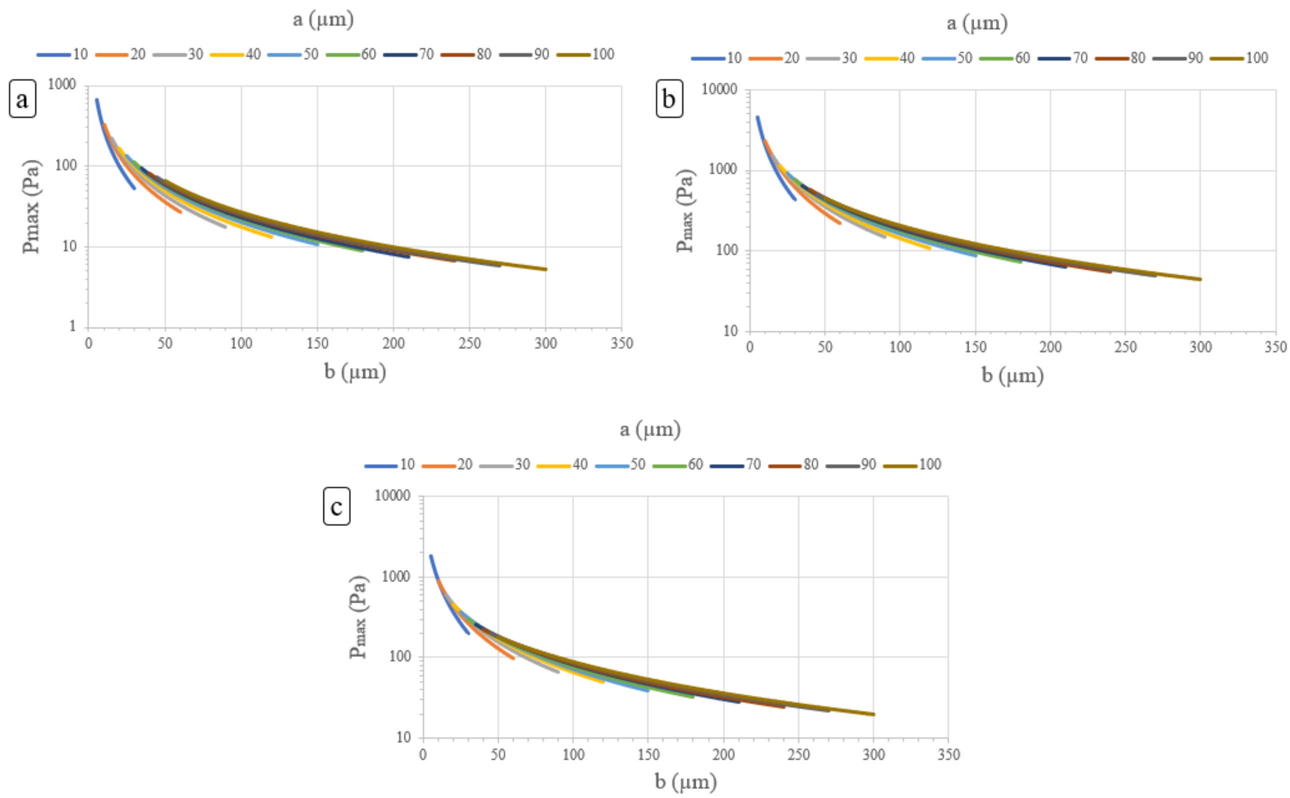

Figure 10. P_{max} as a function of pitch distance (b, µm) for various (a) micropillar top diameters of M2, (b) micropillar top diameters of M3, and (c) the long diagonal of hexagons for M4 geometries

4. Conclusion

A robust and durable non-wetting regime where the transition from a Cassie–Baxter state to a Wenzel state does not occur easily is a highly sought-after goal in the field of superhydrophobic materials. Hierarchical structures are surface geometries that demonstrate durable superhydrophobicity; however, the fabrication procedure of such surfaces is complex. In this paper, we fabricated hierarchical micro-microstructure geometries on silicone rubber surfaces using an industrially applicable, direct-replication method via a micro-compression molding system. Various insert fabrication techniques, including photochemical milling, laser ablation, and wet chemical etching, created well-ordered structures comprising various hierarchical levels. We predicted the dominant wetting regime for each produced surface using thermodynamic equations and roughness parameters. We then calculated the theoretical water contact angle using the predicted wetting regime. We obtained a good agreement between the calculated theoretical wettability properties and the experimental measurements. Finally, we considered the balance between the exerted pressure by water droplets and the capillary force to predict the microstructure dimensions at critical conditions for each surface geometry. Our research team is currently evaluating the influence of droplet impact on the persistence of the

Cassie–Baxter state across superhydrophobic surfaces covered by hierarchical, well-ordered structures.

Acknowledgment

We acknowledge the financial support from the Natural Sciences and Engineering Research Council of Canada (NSERC).

5. References

[1] M. Liravi, H. Pakzad, A. Moosavi, and A. Nouri-Borujerdi, "A comprehensive review on recent advances in superhydrophobic surfaces and their applications for drag reduction," *Progress in Organic Coatings,* vol. 140, p. 105537, 2020.

[2] G. B. Darband, M. Aliofkhazraei, S. Khorsand, S. Sokhanvar, and A. Kaboli, "Science and engineering of superhydrophobic surfaces: review of corrosion resistance, chemical and mechanical stability," *Arabian Journal of Chemistry,* vol. 13, no. 1, pp. 1763-1802, 2020.

[3] A. Hooda, M. Goyat, J. K. Pandey, A. Kumar, and R. Gupta, "A review on fundamentals, constraints and fabrication techniques of superhydrophobic coatings," *Progress in Organic Coatings,* vol. 142, p. 105557, 2020.

[4] P. Nguyen-Tri *et al.*, "Recent progress in the preparation, properties and applications of superhydrophobic nano-based coatings and surfaces: A review," *Progress in Organic Coatings,* vol. 132, pp. 235-256, 2019.

[5] K. Maghsoudi, E. Vazirinasab, G. Momen, and R. Jafari, "Advances in the fabrication of superhydrophobic polymeric surfaces by polymer molding processes," *Industrial and Engineering Chemistry Research,* vol. 59, no. 20, pp. 9343-9363, 2020.

[6] G. Wang, W. Zhou, J. Zhou, M. Wang, Y. Zhang, and H. Qiang, "Superhydrophobic silicone rubber surface prepared by direct replication," *Surface Engineering,* pp. 1-10, 2020.

[7] Y. Liu *et al.*, "Design and preparation of biomimetic polydimethylsiloxane (PDMS) films with superhydrophobic, self-healing and drag reduction properties via replication of shark skin and SI-ATRP," *Chemical Engineering Journal,* vol. 356, pp. 318-328, 2019.

[8] K. Maghsoudi, G. Momen, R. Jafari, and M. Farzaneh, "Direct replication of micro-nanostructures in the fabrication of superhydrophobic silicone rubber surfaces by compression molding," *Applied Surface Science,* vol. 458, pp. 619-628, 2018.

[9] N. K. Andersen and R. Taboryski, "Multi-height structures in injection molded polymer," *Microelectronic Engineering,* vol. 141, pp. 211-214, 2015.

[10] S. F. Toosi, S. Moradi, M. Ebrahimi, and S. G. Hatzikiriakos, "Microfabrication of polymeric surfaces with extreme wettability using hot embossing," *Applied Surface Science,* vol. 378, pp. 426-434, 2016.

[11] H. Peng, Z. Luo, L. Li, Z. Xia, J. Du, and B. Zheng, "Facile fabrication of superhydrophobic aluminum surfaces by chemical etching and its anti-icing/self-cleaning performances," *Materials Research Express,* vol. 6, no. 9, p. 096586, 2019.

[12] R. Sun *et al.*, "Robust superhydrophobic aluminum alloy surfaces with anti-icing ability, thermostability, and mechanical durability," *Progress in Organic Coatings,* vol. 147, p. 105745, 2020.

[13] Y.-P. Zhang *et al.*, "Facile fabrication of superhydrophobic copper-foam and electrospinning polystyrene fiber for combinational oil–water separation," *Polymers,* vol. 11, no. 1, p. 97, 2019.

[14] Z. Tang, M. He, B. Xu, C. Lu, L. Meng, and H. Liu, "Tunable Adhesion on Superhydrophobic Copper Surfaces Using a Facile Controllable Dewetting Approach," *Advanced Materials Interfaces,* vol. 7, no. 8, p. 1902144, 2020.

[15] C. Du, X. He, F. Tian, X. Bai, and C. Yuan, "Preparation of superhydrophobic steel surfaces with chemical stability and corrosion," *Coatings,* vol. 9, no. 6, p. 398, 2019.

[16] J.-H. Kim, A. Mirzaei, H. W. Kim, and S. S. Kim, "Facile fabrication of superhydrophobic surfaces from austenitic stainless steel (AISI 304) by chemical etching," *Applied Surface Science,* vol. 439, pp. 598-604, 2018.
[17] K. Maghsoudi, R. Jafari, G. Momen, and M. Farzaneh, "Micro-nanostructured polymer surfaces using injection molding: A review," *Materials Today Communications,* vol. 13, pp. 126-143, 2017.
[18] J.-Y. So and W.-G. Bae, "Fabrication of superhydrophobic metallic surface by wire electrical discharge machining for seamless roll-to-roll printing," *Metals,* vol. 8, no. 4, p. 228, 2018.
[19] C. Liu *et al.*, "Design of superhydrophobic pillars with robustness," *Surface and Coatings Technology,* vol. 361, pp. 342-348, 2019.
[20] J. Noh, J.-H. Lee, S. Na, H. Lim, and D.-H. Jung, "Fabrication of hierarchically micro-and nano-structured mold surfaces using laser ablation for mass production of superhydrophobic surfaces," *Japanese Journal of Applied Physics,* vol. 49, no. 10R, p. 106502, 2010.
[21] T. Jiang *et al.*, "Ultrashort picosecond laser processing of micro-molds for fabricating plastic parts with superhydrophobic surfaces," *Applied Physics A,* vol. 108, no. 4, pp. 863-869, 2012.
[22] R. Roy, D. Allen, and O. Zamora, "Cost of photochemical machining," *Journal of Materials Processing Technology,* vol. 149, no. 1-3, pp. 460-465, 2004.
[23] J. Zhang and Y. Meng, "A study of surface texturing of carbon steel by photochemical machining," *Journal of Materials Processing Technology,* vol. 212, no. 10, pp. 2133-2140, 2012.
[24] S. S. Wangikar, P. K. Patowari, R. D. Misra, and N. D. Misal, "Photochemical machining: a less explored non-conventional machining process," in *Non-Conventional Machining in Modern Manufacturing Systems*: IGI Global, 2019, pp. 188-201.
[25] D. M. Allen, "Photochemical machining: from 'manufacturing's best kept secret'to a $6 billion per annum, rapid manufacturing process," *CIRP Annals,* vol. 53, no. 2, pp. 559-572, 2004.
[26] M. Zhou, X. Xiong, B. Jiang, and C. Weng, "Fabrication of high aspect ratio nanopillars and micro/nano combined structures with hydrophobic surface characteristics by injection molding," *Applied Surface Science,* vol. 427, pp. 854-860, 2018.
[27] K. Mielonen and T. A. Pakkanen, "Superhydrophobic hierarchical three-level structures on 3D polypropylene surfaces," *Journal of Micromechanics and Microengineering,* vol. 29, no. 2, p. 025006, 2019.
[28] C. Weng, F. Wang, M. Zhou, D. Yang, and B. Jiang, "Fabrication of hierarchical polymer surfaces with superhydrophobicity by injection molding from nature and function-oriented design," *Applied Surface Science,* vol. 436, pp. 224-233, 2018.
[29] E. Huovinen, J. Hirvi, M. Suvanto, and T. A. Pakkanen, "Micro–micro hierarchy replacing micro–nano hierarchy: a precisely controlled way to produce wear-resistant superhydrophobic polymer surfaces," *Langmuir,* vol. 28, no. 41, pp. 14747-14755, 2012.
[30] I. Saarikoski, F. Joki-Korpela, M. Suvanto, T. T. Pakkanen, and T. A. Pakkanen, "Superhydrophobic elastomer surfaces with nanostructured micronails," *Surface Science,* vol. 606, no. 1-2, pp. 91-98, 2012.
[31] F. Chen *et al.*, "Creating robust superamphiphobic coatings for both hard and soft materials," *Journal of Materials Chemistry A,* vol. 3, no. 42, pp. 20999-21008, 2015.
[32] A.-C. Liou and R.-H. Chen, "Injection molding of polymer micro-and sub-micron structures with high-aspect ratios," *The International Journal of Advanced Manufacturing Technology,* vol. 28, no. 11-12, pp. 1097-1103, 2006.
[33] C.-H. Lim, S.-Y. Han, J.-D. Eo, K. Kim, and W.-B. Kim, "Superhydrophobic hierarchical structures produced through novel low-cost stamp fabrication and hot embossing of thermoplastic film," *Journal of Mechanical Science and Technology,* vol. 29, no. 12, pp. 5107-5111, 2015.
[34] M. Röhrig *et al.*, "Hot pulling and embossing of hierarchical nano-and micro-structures," *Journal of Micromechanics and Microengineering,* vol. 23, no. 10, p. 105014, 2013.
[35] K. Mielonen, M. Suvanto, and T. Pakkanen, "Curved hierarchically micro–micro structured polypropylene surfaces by injection molding," *Journal of Micromechanics and Microengineering,* vol. 27, no. 1, p. 015025, 2016.

[36] A. Peters *et al.*, “Cassie–Baxter to Wenzel state wetting transition: Scaling of the front velocity,” *The European Physical Journal E,* vol. 29, no. 4, pp. 391-397, 2009.
[37] C. E. Cansoy, H. Y. Erbil, O. Akar, and T. Akin, “Effect of pattern size and geometry on the use of Cassie–Baxter equation for superhydrophobic surfaces,” *Colloids Surfaces A: Physicochemical Engineering Aspects,* vol. 386, no. 1-3, pp. 116-124, 2011.
[38] H. S. Grewal, I.-J. Cho, J.-E. Oh, and E.-S. Yoon, “Effect of topography on the wetting of nanoscale patterns: experimental and modeling studies,” *Nanoscale,* vol. 6, no. 24, pp. 15321-15332, 2014.
[39] N. A. Patankar, “Transition between superhydrophobic states on rough surfaces,” *Langmuir,* vol. 20, no. 17, pp. 7097-7102, 2004.
[40] H. Grewal, S. Piao, I.-J. Cho, K.-Y. Jhang, and E.-S. Yoon, “Nanotribological and wetting performance of hierarchical patterns,” *Soft Matter,* vol. 12, no. 3, pp. 859-866, 2016.
[41] V. Hejazi, A. D. Moghadam, P. Rohatgi, and M. Nosonovsky, “Beyond Wenzel and Cassie–Baxter: second-order effects on the wetting of rough surfaces,” *Langmuir,* vol. 30, no. 31, pp. 9423-9429, 2014.
[42] B. Hou, C. Wu, X. Li, J. Huang, and M. Chen, “Contact line-based model for the Cassie-Wenzel transition of a sessile droplet on the hydrophobic micropillar-structured surfaces,” *Applied Surface Science,* vol. 542, p. 148611.
[43] Y. Zhao, H. Zhang, W. Wang, and C. Yang, “Wetting transition of sessile and condensate droplets on copper-based superhydrophobic surfaces,” *International Journal of Heat and Mass Transfer,* vol. 127, pp. 280-288, 2018.
[44] N. Okulova, P. Johansen, L. Christensen, and R. Taboryski, “Effect of structure hierarchy for superhydrophobic polymer surfaces studied by droplet evaporation,” *Nanomaterials,* vol. 8, no. 10, p. 831, 2018.
[45] A. Sudeepthi, L. Yeo, and A. Sen, “Cassie–Wenzel wetting transition on nanostructured superhydrophobic surfaces induced by surface acoustic waves,” *Applied Physics Letters,* vol. 116, no. 9, p. 093704, 2020.
[46] A. A. Yancheshme, S. Hassantabar, K. Maghsoudi, S. Keshavarzi, R. Jafari, and G. Momen, “Integration of experimental analysis and machine learning to predict drop behavior on superhydrophobic surfaces,” *Chemical Engineering Journal,* p. 127898, 2020.
[47] L. Huang, Y. Yao, Z. Peng, B. Zhang, and S. Chen, “How to Achieve a Monostable Cassie State on a Micropillar-Arrayed Superhydrophobic Surface,” *The Journal of Physical Chemistry B,* 2021.
[48] W. Ren, “Wetting transition on patterned surfaces: transition states and energy barriers,” *Langmuir,* vol. 30, no. 10, pp. 2879-2885, 2014.
[49] W. Gong, Y. Zu, S. Chen, and Y. Yan, “Wetting transition energy curves for a droplet on a square-post patterned surface,” *Science Bulletin,* vol. 62, no. 2, pp. 136-142, 2017.
[50] D. Murakami, H. Jinnai, and A. Takahara, “Wetting transition from the Cassie–Baxter state to the Wenzel state on textured polymer surfaces,” *Langmuir,* vol. 30, no. 8, pp. 2061-2067, 2014.
[51] T. Young, “III. An essay on the cohesion of fluids,” *Philosophical Transactions of the Royal Society of London,* no. 95, pp. 65-87, 1805.
[52] R. N. Wenzel, “Resistance of solid surfaces to wetting by water,” *Industrial and Engineering Chemistry,* vol. 28, no. 8, pp. 988-994, 1936.
[53] A. Cassie and S. Baxter, “Wettability of porous surfaces,” *Transactions of the Faraday Society,* vol. 40, pp. 546-551, 1944.
[54] B. K. Nayak, P. O. Caffrey, C. R. Speck, and M. C. Gupta, “Superhydrophobic surfaces by replication of micro/nano-structures fabricated by ultrafast-laser-microtexturing,” *Applied Surface Science,* vol. 266, pp. 27-32, 2013.
[55] K. Maghsoudi, E. Vazirinasab, R. Jafari, and G. Momen, “Evaluating the effect of processing parameters on the replication quality in the micro compression molding of silicone rubber,” *Materials and Manufacturing Processes,* pp. 1-9, 2020.
[56] M. A. R. Khandoker and K. Golovin, “Statistical Heuristic Wettability Analysis of Randomly Textured Surfaces,” *Langmuir,* vol. 36, no. 47, pp. 14361-14371, 2020.

[57] L. Feng *et al.*, "Petal effect: a superhydrophobic state with high adhesive force," *Langmuir,* vol. 24, no. 8, pp. 4114-4119, 2008.
[58] P. Fan, R. Pan, and M. Zhong, "Ultrafast Laser Enabling Hierarchical Structures for Versatile Superhydrophobicity with Enhanced Cassie–Baxter Stability and Durability," *Langmuir,* vol. 35, no. 51, pp. 16693-16711, 2019.
[59] W. Li, A. J. A. i. c. Amirfazli, and i. science, "Microtextured superhydrophobic surfaces: A thermodynamic analysis," *Advances in Colloid and Interface Science,* vol. 132, no. 2, pp. 51-68, 2007.

[60] Zhang, J., Rosenkranz, A., Zhang, J., Guo, J., Li, X., Chen, X., ... & Xu, J. (2022). Modified wettability of micro-structured steel surfaces fabricated by elliptical vibration diamond cutting. International Journal of Precision Engineering and Manufacturing-Green Technology, 9(5), 1387-1397.